Journal of Materials Chemistry A

ROYAL SOCIETY OF CHEMISTRY

PAPER

View Article Online
View Journal | View Issue

Cite this: J. Mater. Chem. A, 2021, 9, 21379

Facile fabrication of micro-/nanostructured, superhydrophobic membranes with adjustable porosity by 3D printing†

Fadoua Mayoussi, [a] Egan H. Doeven, [d] Andrea Kick, [a] Andreas Goralczyk, [a] Yi Thomann, [bc] Patrick Risch, [a] Rosanne M. Guijt, [d] Frederik Kotz, [ab] Dorothea Helmer *[abc] and Bastian E. Rapp [abc]

Porous membranes with special wetting properties have attracted great interest due to their various functions and wide applications, including water filtration, selective oil/water separation and oil skimming. Special wetting properties such as superhydrophobicity can be achieved by controlling the surface chemistry as well as the surface topography of a substrate. Three-dimensional (3D) printing is a promising method for the fast and easy generation of various structures. The most common method for 3D printing of superhydrophobic materials is a two-step fabrication process: 3D printing of user-defined topographies, such as surface structures or bulk porosity, followed by a chemical post-processing with low-surface energy chemicals such as fluorinated silanes. Another common method is using a hydrophobic polymer ink to print intricate surface structures. However, the resolution of most common printers is not sufficient to produce nano-/microstructured textures, moreover, the resulting delicate surface micro- or nanostructures are very prone to abrasion. Herein, we report a simple approach for 3D printing of superhydrophobic micro-/nanoporous membranes in a single step, combining the required topography and chemistry. The bulk porosity of this material, which we term "Fluoropor", makes it insensitive to abrasion. To achieve this, a photocurable fluorinated resin is mixed with a porogen mixture and 3D printed using a stereolithography (SLA) printing process. This way, micro-/nanoporous membranes with superhydrophobic properties with static contact angles of 164° are fabricated. The pore size of the membranes can be adjusted from 30 nm to 300 nm by only changing the porogen ratio in the mixture. We show the applicability of the printed membranes for oil/water separation and the formation of *Salvinia* layers which are of great interest for drag reduction in maritime transportation and fouling prevention.

Received 21st April 2021
Accepted 22nd August 2021

DOI: 10.1039/d1ta03352b

rsc.li/materials-a

Introduction

Porous membranes with special wetting properties, such as superhydrophobicity have lately attracted considerable attention. These surfaces are described by a static water contact angle greater than 150°, a roll-off angle smaller than 10° and are widely used for anti-fouling coatings,[1] anti-icing surfaces[2] or oil/water separation.[3,4] Manufacturing of such membranes requires structuring of surfaces on a nano- to microscale. The micro-/nanostructure or roughness promotes the formation of residual air pockets (*Salvinia* layer, *i.e.* Cassie wetting state), that cause the decrease in the roll-off angle, and adhesive force.[5–9] Unfortunately, this delicate surface structuring makes most superhydrophobic surfaces very sensitive to abrasion and renders them impractical for real-life applications. The most common process for producing such structures is a top-down approach, where defined micro-/nano-scale surface topographies are coated with a low-surface energy chemical such as fluorinated silanes.[10–12] In practice, often porous supports, typically mesh substrates are coated by hydrophobic materials.[13,14] Common problems associated with this method are the poor adhesion between the mesh and the built-up hydrophobic layer leading to delamination and abrasion, and the clogging of the mesh pores during the post chemical modification of the surface. Another fabrication strategy is bottom-up structuring of a material with low surface energy using

[a]Laboratory of Process Technology, NeptunLab, Albert-Ludwigs University Freiburg, Department of Microsystems Engineering (IMTEK), Georges-Köhler-Allee 103, Freiburg, Germany. E-mail: dorothea.helmer@neptunlab.org; Web: www.NeptunLab.org

[b]Freiburg Materials Research Center (FMF), Albert-Ludwigs-University Freiburg, Freiburg, Germany

[c]FIT Freiburg Centre for Interactive Materials and Bioinspired Technologies, Albert-Ludwigs University, Freiburg, Germany

[d]Deakin University, Centre for Regional and Rural Futures, Geelong, VIC, 3220, Australia

† Electronic supplementary information (ESI) available. See DOI: 10.1039/d1ta03352b

processes such as, *e.g.*, chemical vapor deposition, sol–gel methods and layer-by-layer deposition.[15–19] The most common class of materials used are fluorinated polymers due to their unique chemical and physical properties such as low polarizability, low adhesion as well as high chemical resilience, *e.g.*, against corrosive liquids. Moreover, fluorine-rich polymers possess low surface energies, which endow their surfaces with excellent water and oil repellency.[20–22]

Due to its versatility and ease in generating complex shapes with geometrical features, three-dimensional printing (3D printing) has emerged as a promising technology to prepare porous structures.[23–29] However, due to the limitations in resolution and adjustability of pore size, the fabrication of micro/nanostructured membranes *via* 3D printing remains challenging. In 3D printing processes, top-down approaches are commonly employed, where the patterned geometry is printed and the resultant surface structure is then chemically modified with low surface energy compounds. Fused deposition modelling (FDM),[30] selective laser sintering (SLS)[31] and direct inkjet writing (DIW)[32] are the most common methods for preparing superhydrophobic porous membranes. Recently, Lv *et al.* reported the fabrication of superhydrophobic porous membranes for oil/water separation by 3D printing an ordered mesh structure using an ink of polydimethylsiloxane (PDMS) and hydrophobic silica particles with pore sizes in the sub-millimeter range.[32] Yuan *et al.* reported the fabrication of polysulfone membranes *via* SLS and their application for oil/water separation. The printed porous membranes were subsequently coated with candle soot to achieve superhydrophobicity.[33] They also reported the fabrication of a micro-/nanostructural surface by designing a unique 3D multiscale zeolitic imidazolate framework (ZIF-L) on a 3D printed membrane for a superhydrophobic and underwater superoleophobic surface.[34] However, these reported methods enable only the formation of large pores in the micrometer range, lacking the required combined micro-/nanostructure and still requiring additional surface modifications to achieve superhydrophobicity. Besides, the pore size plays an important role in membrane applications in various fields from separation, adsorption to tissue engineering.[14,31–33,35–38] Thus, a method for adjusting the porous structure is of high interest. Polymerization induced phase separation (PIPS) has emerged as a promising method to address these limitations as it offers the possibility to create materials with inherent, self-organized porous structure with adjustable porosity.[20,39–42] As of late, it has been effectively applied in the fabrication of micro/-nanoporous materials, such as glass and polymers, using SLA.[43–47]

In this paper, we report the SLA 3D printing of thin superhydrophobic membranes (100–400 μm) with adjustable porosity in the submicron range with 30 nm to 300 nm pores. The process combines both, required topography and surface chemistry for achieving superhydrophobicity in a single step. For achieving this, a photocurable fluorinated resin is mixed with a non-solvent to create a micro-/nanostructure throughout the bulk by phase separation during polymerization. The resin is then printed into a special "staircase" design, which with help of the layer-by-layer nature of the SLA printing process, enables exposing the micro-/nanostructure of the membranes by peeling off thin layers from the bulk. Superhydrophobic membranes with a static water contact angle of 164° are thus obtained with no need of further surface modifications. The printed membranes were successfully applied as oil/water separators, oil absorbers/skimmers and for the detection and potential regeneration of *Salvinia* layers.

Experimental

Materials

Fluorolink MD700 (a perfluoropolyether (PFPE)-methacrylate) was purchased from Acota (United Kingdom), 1*H*,1,2*H*,2*H*-perfluorooctanol (13FOOl) was purchased from Apollo Scientific (United Kingdom). Diphenyl(2,4,6-trimethylbenzoyl)phosphine oxide (TPO) and Sudan 3 were purchased from Sigma-Aldrich (Germany). Cyclohexanol, cyclohexane and chloroform were purchased from Merck (Germany). Acetone and 2-propanol were purchased from Carl Roth (Germany). Tinuvin 384-2 was kindly provided by BASF (Germany).

Preparation of the porous Fluoropor membranes

Synthesis of the polymer mixture Fluorolink MD700 (50 wt%) was mixed with a porogen mixture consisting of a non-solvent (cyclohexanol) and an emulsifying agent (13FOOl). The porogen mixture is used to create the micro-/nano porous network in the polymerized parts.[18] The amount of the non-solvent and the emulsifying agent vary in dependence of the desired pore size of the membrane. The monomer–porogen mixture was then blended with 0.5 wt% of the photoinitiator TPO. In the case of the polymer mixture used for the 3D printing of the staircase design, the absorber Tinuvin 384-2 0.6 wt% was added. The mixture was sonicated for 15 min using an ultrasonic bath to dissolve the initiator.

3D printing of the membranes for the 3D printing process, an Asiga Pico 2 SLA printer (Asiga, Australia) with a building platform of 39.7 × 63.6 mm^2 and a light intensity of 88 W m^{-2} as well as a Phrozen shuffle 4K SLA printer (Phrozen Tech Co. Ltd, Taiwan) with a build platform of 67.6 × 120 mm^2 and a light intensity of 3 W m^{-2} were used. The single layer of the printed Fluoropor membrane stacks was 100 μm. To avoid the delamination of the layers during the print process, the *z*-compensation was set to 150 μm. Whereas for the staircase designs printed in the Asiga Pico 2, the single layer thickness was 200 μm and the *z*-compensation was set at 0 μm to allow an easy peeling off the layers. A burn-in layer of 300 μm was required to avoid the delamination of the print from the platform.

The prints were placed in 2-propanol overnight and dried at room temperature for 8–16 h to wash away and remove the porogen and residual resin. The required drying time depends on the thickness of the prints. The prints were dried afterwards at 100 °C for 30 min under vacuum with a pressure of 50 mbar to ensure a complete removal of any solvent and porogen residue. Single and multiple layers could be easily peeled off the staircase design using a laboratory tweezer exposing the patterned

structure responsible for the superhydrophobicity of the membranes (see Fig. 1).

Characterizations

Scanning electron microscopy (SEM) measurements

The top surface and cross-section of the membranes were firstly sputtered with a 10–20 nm gold layer under an argon atmosphere and then visualized by SEM (Quanta 250 FEG, Thermo Fisher scientific, Germany) and high-resolution focused ion beam SEM of type Scios 2 DualBeam (Thermo Fisher Scientific).

Analysis of pore size distribution

The pore size distribution was measured *via* image analysis of cross-sectional SEM images using ImageJ. Prior to the SEM measurements, the printed membrane stacks were embedded into PDMS to fix them and avoid deformation. Subsequently, thin even cross-sectional layers (1 μm) were cut using a cryo ultramicrotome (Leica microsystems).

SEM images of the cut layer's surface were taken, and the pore size distribution was determined by using the threshold function followed by the analysis of the Feret diameters of the pores.

Contact angle (CA) measurements

The contact angles of the surfaces were measured with an OCA 15Pro (Data Physics, Germany). Static contact angles were measured using 5 μL water droplets at room temperature following the sessile droplet method. Three contact angles were measured at three different positions on the membrane surface and were used for calculating the average values.

Measurement of the layer thickness

The thicknesses of the disc membrane stacks and peeled-off membrane layers were determined using a length gauge of type MT 60M (Heidenhain, Germany).

Oil/water separation

For the separation of water and oil mixtures, a lab customized device consisting of a funnel and a metal filter with large pores was used. The membrane was placed on top of the metal filter and the whole setup was fixed with a clip. The membranes were first pre-wetted with cyclohexane. Mixtures of cyclohexane or chloroform and water (1 : 1, v/v) were prepared by stirring for 5 min. These mixtures were slowly poured onto the membranes and the separation was achieved by pulling vacuum. In order to distinguish the liquids, water was dyed blue using a food colorant. The separation efficiency (η) was calculated according to the following equation:

$$\eta = \frac{m_a}{m_b} \times 100 \quad (1)$$

here η is the separation efficiency and m_a and m_b refer to the mass of the water after and before separation, respectively.

Mechanical stability of the thin superhydrophobic membranes

The stability of the superhydrophobic properties was examined by measuring the water contact angles of the membranes after mechanical damage tests, such as stretching and two-point bending tests.

Detection of the *Salvinia* layer

To demonstrate the detection of the *Salvinia* layer, thin Fluoropor 15 membranes (directly printed and peeled off the staircase design) were glued on a glass slide and submerged partially in a water bath to visualize the *Salvinia* layer. The volume of the retained air layer (*i.e.*, the *Salvinia* layer) was also quantified by comparing the volume of the directly printed membrane that does not expose the micro-/nanostructure ("closed surface" without *Salvinia* layer) and the peeled membrane off the staircase design, which exposes the micro-/nanostructure ("open surface" with the *Salvinia* layer). Four samples with four different sizes from both membranes were prepared for these experiments. The density of the membranes was measured according to Archimedes principle using an analytical balance (QUINTIX 124-1S) in combination with a density determination set YDK03 (SARTORIUS AG, Germany). The *Salvinia* layer volume was calculated using the following equation:

$$V_{\text{salvinia}} = \frac{m_o(\text{dry}) - m_o(\text{under water})}{\rho_0} - \frac{m_o}{\rho_c} \quad (2)$$

where, V_{salvinia} is the volume of the air layer, m_o is the mass of the open membrane, ρ_0 is the density of water at the given temperature and ρ_c is the density of the closed membrane. The dependence of the membrane surface area on the volume of the *Salvinia* air layer was plotted.

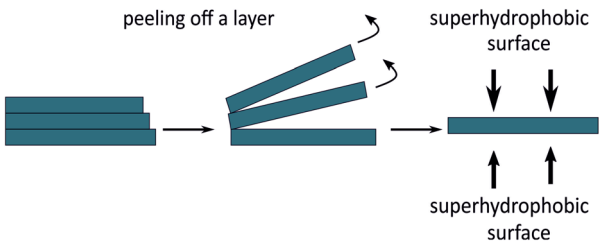

Fig. 1 Schematic of the peeling off process that enables exposing the nano\-microstructure of the membrane on both top and bottom surface.

Results and discussion

Fabrication of directly printed membranes for oil/water separation

For direct 3D printing of micro-/nanostructured membranes, two different mixtures for generating Fluoropor fluorinated polymer foams were formulated. With these resin mixtures, a micro-/nanostructure can be achieved throughout the printed material, due to a phase-separation of the resin during the printing process. This way, a much smaller pore size of the

membranes can be achieved compared to the feature resolution commonly achieved by SLA. By introducing different amounts of non-solvent and stabilizing the monomer/non-solvent mixture by an emulsifying agent, two stable printing resins mixtures were generated, termed Fluoropor 15 and Fluoropor 25 (see Table 1).

Using these resins, an SLA printing process was used to produce custom-shaped membranes. Using the Asiga Pico 2, membranes disc of 35 mm diameter, consisting of several printed layers with an overall thickness of 500 μm were printed. These "membrane stacks" possess different pore volumes, as indicated by the different optical appearance of the membranes, ranging from translucent in case of Fluoropor 15 to white and non-transparent in case of Fluoropor 25 (Fig. 2). A higher content of non-solvent generates a larger overall pore volume that causes the material's appearance to turn from translucent to white and non-transparent. Due to the removal of porogens and material de-swelling, the production process was accompanied by a linear shrinkage of 20% and 14% in the *x*–*y* direction, 32% and 26% in the *z* direction for Fluoropor 15 and Fluoropor 25, respectively. The wetting properties of the membranes were investigated by contact angle measurements. Fluoropor 15 and Fluoropor 25 show a static contact angle of 123 ± 2 °and 126 ± 4°, respectively (see ESI Fig. S1†).

To investigate the structure of the membranes, SEM measurements of the cross-section as well as the top and bottom surface were taken. SEM images of the top- and bottom surfaces of both membranes are shown in Fig. 3. As can be seen, the micro-/nanostructure is not visible on the surfaces but clearly visible in the cross-sections of the membranes (see Fig. 3). In the given SLA setup, the printing process is carried out in a constrained volume between a transparent window (through which the DLP illuminates the build volume) and the build platform. Therefore, the lack of porosity on the surface is a result of the direct contact of the printing resin with the build platform (bottom surface) and the transparent window (top surface). The porosity within the bulk of the material is shown in the cross-section in *z*-direction (see Fig. 3E and F). With an increased amount of the non-solvent, the phase separation occurs faster enabling the formation of thicker polymer networks, and *vice versa*.

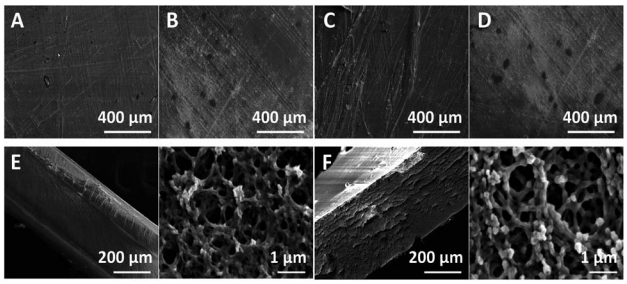

Fig. 3 SEM images of the top surface (*i.e.*, the surface in contact with the printer's transparent window) and bottom surface (*i.e.*, the surface in contact with the printer's build platform) of Fluoropor 15 and 25 membranes and the cross-sections. (A) Bottom surface of Fluoropor 15 membrane, (B) top surface of Fluoropor 15 membrane, (C) bottom surface of Fluoropor 25 membrane, (D) top surface of Fluoropor 25 membrane. (E) Cross-section and close-up of the cross-section of Fluoropor 15 membrane, showing the porosity of the material, (F) cross-section and close-up of Fluoropor 25 membrane.

Table 1 The required amounts of the reactants for the preparation of the resin mixtures

	Fluoropor 15 resin mix	Fluoropor 25 resin mix
Monomer MD700 (wt%)	50	50
Emulsifying agent (wt%)	35	25
Non-solvent (wt%)	15	25
Initiator[a] (mg ml^{-1})	7	7
Absorber[a] (mg ml^{-1})	3.3	3.3

[a] Concentration in Fluoropor mix.

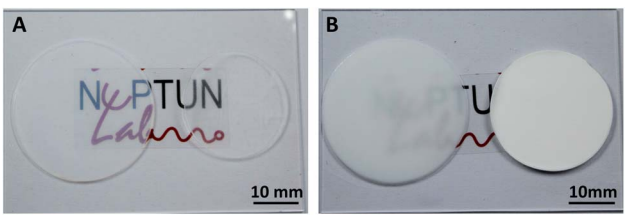

Fig. 2 3D printed disc shaped membrane stacks with a total thickness of 500 μm after printing and after porogen removal. (A) 3D printed Fluoropor 15 membrane stack; (left) directly after printing and (right) shrunken dried membrane stack after porogen removal. (B) 3D printed Fluoropor 25 membrane stack; (left) directly after printing and (right) shrunken dried membrane stack after porogen removal.

The porosity of both membranes was measured from the cross-sectional SEM images *via* image analysis by using a thresholding function and analysis of the pore's diameters using Image J (see ESI Fig. S2†). The pore size distribution is shown in Fig. 4. Fluoropor 15 membrane displays a median pore size of 30 nm whereas Fluoropor 25 membrane displays a median pore size of 300 nm.

Oil/water separation

To investigate, whether the printed membranes are suitable for oil/water separation the membranes were first tested for their

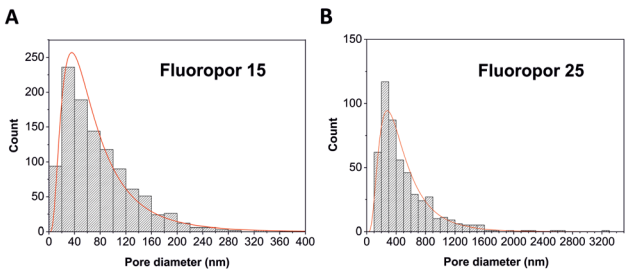

Fig. 4 Plotted pore size distribution of the 3D printed Fluoropor membranes from the cross-sectional SEM images. (A) Fluoropor 15, (B) Fluoropor 25.

capacity to absorb organic solvents (see Fig. 5). Droplets of chloroform and cyclohexane were readily absorbed by Fluoropor 25 membrane, whereas a water droplet was repelled as expected. To test the absorption capacity of both membranes, droplets of different oils and a droplet of water were placed on Fluoropor 15 and Fluoropor 25. Due to its larger pore fraction, Fluoropor 25 absorbed both chloroform and cyclohexane directly, whereas the Fluoropor 15 membrane only partially absorbed the fluids. Thus, for all further separation experiments, Fluoropor 25 membranes were chosen. Disc-shaped membranes with a 45 mm diameter were 3D printed using the Phrozen shuffle 4K and placed into a filter funnel. A mixture of chloroform and water or cyclohexane and water (1 : 1, v/v) was poured into the funnel (Fig. 5B). A low vacuum pressure was applied to the setup to achieve the separation. The separation efficiency of a chloroform–water mixture and a cyclohexane–water mixture using Fluoropor 25 membrane was over 99 ± 1% and 79 ± 2%, respectively (see Fig. 5C). Thus, an efficient separation of chloroform/water mixtures was achieved using the Fluoropor 25 membrane. In addition, the printed membrane can be easily cleaned with 2-propanol or acetone, dried and reused. The membrane stability and efficiency was tested up to 5 cycles with a small reduction of the efficiency within the error of the measurement: separation efficiency for chloroform of 99 ± 1% in cycle 1 and 98 ± 1% in cycle 5 and for cyclohexane of 79 ± 2% in cycle 1 and 74.5 ± 4% in cycle 5 was measured (see Fig. 5D). The collected separated oils were tested for residual water content using an anhydrous copper sulfate color test. Both collected oils did not show any traces of water within the detection limit of 0.01 vol% (see ESI Fig. S3†).

The Fluoropor 25 membrane was also tested for its capacity to absorb crude oil. The membrane was immersed in a vial containing water with crude oil floating on the surface. The membrane started absorbing the crude oil right after being immersed in the vial and successfully absorbed all of it after 3 h (see Fig. 5E). This indicates that Fluoropor 25 membrane can potentially be used for oily wastewater treatments by absorbing the oil spills on the water surface.

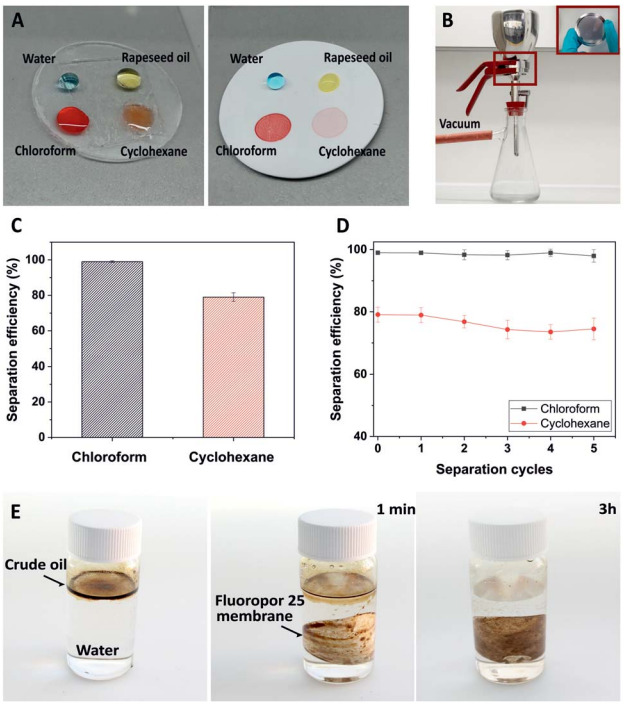

Fig. 5 Liquid absorption by Fluoropor membranes. (A) Photograph of water droplet and different oil droplets on Fluoropor 15 membrane (left) and on Fluoropor 25 membrane (right). (B) The customized lab set-up for the oil/water separation experiment, showing the metallic filter funnel and supporting mesh. (C) The separation efficiency of the Fluoropor 25 membrane for mixtures of water–chloroform and water–cyclohexane. (D) Separation efficiency over 5 separation cycles for water–chloroform and water–cyclohexane mixtures. The membrane was washed after each cycle and reuse. The data show small reduction of efficiency within the error of the measurement (E) absorption of crude oil drop in water. The crude oil was totally absorbed after 3 hours using Fluoropor 25 membrane.

Fabrication of thin superhydrophobic membranes

Via the direct printing process, only membranes with thicknesses higher than 200 μm could be achieved. Due to the shrinkage during drying, thinner membranes were not self-supporting and lost their porosity during the drying process. Thus, another approach was developed, to enable the formation of thin membranes. The layer-by-layer nature of the SLA printing process allows for peeling off individual layers from a bulk printed block, thus generating thin individual membranes. A special printing design was introduced, which facilitates the pulling of individual layers by a slight offset (staircase design) of the printed layers (Fig. 6A and B). By printing Fluoropor 15 and Fluoropor 25 stacks using this design, individual thin membranes of 100 μm and multiple membrane layers of 400 μm thickness could be peeled from the bulk of Fluoropor 15 and Fluoropor 25 block, respectively, after the drying process (Fig. 6C and D). This process enables the

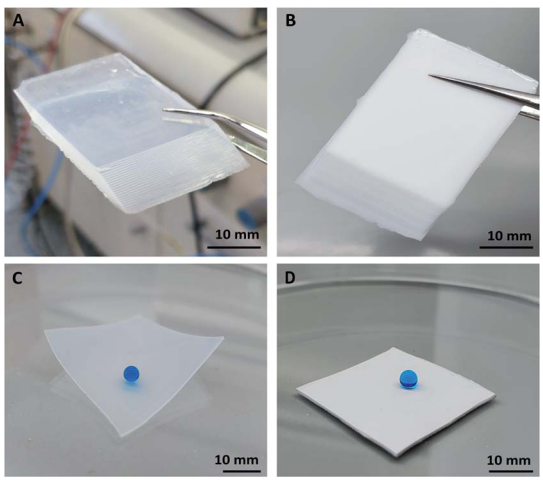

Fig. 6 The 3D printed micro-/nanoporous Fluoropor stacks for membrane preparation. (A) Printed block of Fluoropor 15, (B) printed block of Fluoropor 25. (C) and (D) Peeled-off thin layers of a Fluoropor 15 membrane (C) and Fluoropor 25 membrane (D). A water droplet (dyed blue) is fully repelled by the membrane, showing a static contact angle of 161° for a Fluoropor 15 membrane and 164° for a Fluoropor 25 membrane.

production of 20 membranes in 10 min by peeling individual membranes from a 5 mm stack. Contact angle measurements of the peeled membranes showed that the membranes have superhydrophobic wetting properties with static contact angles of 161 ± 2° and 164 ± 7° for Fluoropor 15 and Fluoropor 25 membranes, respectively (see ESI Fig. S4†). A water droplet is thus fully repelled on the membranes (see Fig. 6C and D).

The superhydrophobic properties suggest an exposed micro-/nanostructure on the peeled membrane's surface. To analyze the bulk structure of the printed block, SEM images of the cross section of several printed layers were taken (see Fig. 7A and B), showing the desired micro-/nanostructure throughout the bulk material. To investigate the peeled membrane top and bottom structure, further SEM images were taken (Fig. 7C–F), clearly showing the micro-/nanostructure of the material. A slight increase in the polymer network features sizes are observed for Fluoropor 25.

Mechanical stability of the thin superhydrophobic membranes

The mechanical stability of the thin superhydrophobic membranes was evaluated by applying mechanical stress (stretching and bending tests). A stress–strain test was performed to evaluate the maximal strain for both membranes before breaking. For Fluoropor 15 membranes and for Fluropor 25 membranes the maximum strain is 22% and 32% respectively (see ESI Fig. S5†).

To assess the influence of mechanical stress on the performance of the membranes, the static contact angle of water on the membranes was measured after 50, 100, 150, 300 and 500 stretching and bending cycles. Both membranes retain their superhydrophobic properties after 500 bending and stretching–releasing cycles with a strain of 20% for Fluoropor 15 and 25% for Fluoropor 25 membranes (see Fig. 8). This high stability is a promising result for using such membranes under real-world conditions.

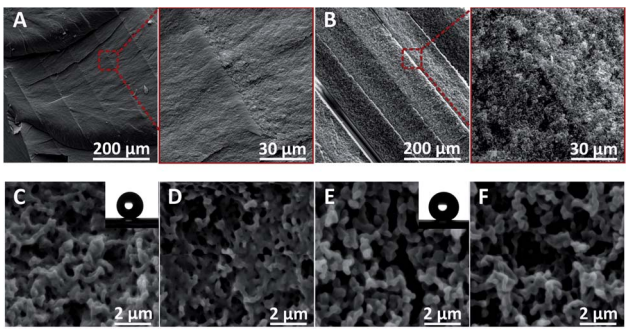

Fig. 7 SEM images of the bulk cross-sections and the peeled Fluoropor membranes' top and bottom surfaces. (A) Fluoropor 15 cross-section and close-up, (B) Fluoropor 25 cross-section and close-up. The membranes show bulk porosity as well as on the surface, rendering them superhydrophobic. (C) Fluoropor 15 membrane top surface, (D) Fluoropor 15 membrane bottom surface, (E) Fluoropor 25 membrane top surface, (F) Fluoropor 25 membrane bottom surface.

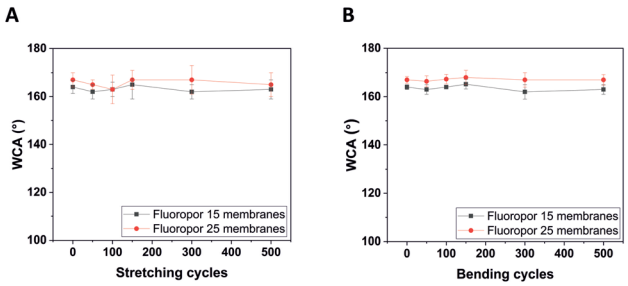

Fig. 8 Mechanical stability tests of the peeled superhydrophobic membranes under stretching and bending. (A) Static water contact angles (WCA) of the membranes after 500 stretching–releasing cycles show an unaffected membrane performance, with the membranes retaining a water contact angle of >162°. (B) WCAs of the membranes after 500 bending cycles show an unaffected membrane performance, with the membranes retaining a water contact angle of >163°.

Detection of the *Salvinia* layer

Thin, superhydrophobic membranes can be exploited for generating a stable air layer under water (*Salvinia* effect) under static conditions. This air retention capability is technologically interesting as the retained air layer reduces drag force and prevents biofouling. To test the formation of a *Salvinia* layer on the membranes, a peeled Fluoropor 15 membrane, which exposes the micro/-nanostructure and a directly printed Fluoropor 15 membrane, which doesn't expose the micro/-nanostructure were glued on a glass slide. When the membranes were immersed under water, an air film was trapped in the micro-/nanostructure of the membrane forming a *Salvinia* layer, which was recognized by the silvery reflective layer on the peeled superhydrophobic membrane. In contrast, no change was noticed on the directly printed hydrophobic membrane when submerged under water (see Fig. 9A). The volume of the different membranes was calculated by the Archimedes principle (see Fig. 9B). The volume of the retained

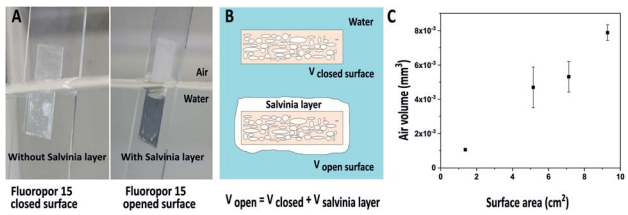

Fig. 9 Visualization and quantification of the *Salvinia* layer formation on Fluoropor 15. (A) A directly printed Fluoropor 15 membrane and a peeled-off Fluoropor 15 membrane were glued on a glass slide and partially submerged under water; the submerged area of the peeled membrane shows a silvery layer which indicated the trapped *Salvinia* layer whereas the color of the non-submerged area did not change. (B) The volume of the *Salvinia* layer was calculated by the Archimedes principle – a schematic of both directly printed and peeled Fluoropor 15 membrane under water shows the difference in displayed water volume by the *Salvinia* layer. (C) Change of the volume of *Salvinia* layer in dependence of the membrane surface area. The data suggests an air volume of ~6 mm^3 per 7 cm^2 of surface area, which corresponds to a Salvinia layer of ~9 ± 1 µm thickness.

air layer (*Salvinia* layer) varies in dependence of the surface area of the membrane in a near linear increase. The larger the surface area of the membrane is the higher the trapped air volume (see Fig. 9C). The data suggests an air volume of $\sim$6 mm^3 per 7 cm^2 of surface area, which corresponds to a *Salvinia* layer of $\sim 9 \pm 1$ μm thickness.

Conclusion

In summary, we have shown a convenient methodology to produce porous membranes in a highly fluorinated polymer with adjustable submicron porosity *via* 3D printing using a commercially available SLA printer. The pore size can be simply adjusted by varying the amount of the non-solvent in the polymer mixture. The as-printed membranes manifest hydrophobic wetting properties with static contact angles in the range of 126°. Due to their bulk porosity and hydrophobicity, the printed membranes with an average pore size above 100 nm achieved an excellent oil–water separation efficiency of over 99% for chloroform/water mixtures. Besides, thin superhydrophobic membranes with adjustable porosity were successfully fabricated by peeling thin layers from a bulk print with a special design that we developed to facilitate layer separation. The peeled membranes showed superhydrophobic wetting properties with a static contact angle in the range of 164°. While submerging the thin superhydrophobic membranes in water, a *Salvinia* layer was formed trapping an air film between the micro-/nanostructure of the membrane and water. The presented membrane fabrication enables the facile generation of customized membranes for applications such as, *e.g.*, oil/water separation. Through their porous nature these superhydrophobic thin membranes can be potentially used for the stabilization and regeneration of a *Salvinia* layers in dynamic modus.

Conflicts of interest

The authors declare no conflict of interest.

Acknowledgements

This work was funded by the German Ministry of Education and Research (BMBF), funding code 03X5527 "Fluoropor" and the German Academic Exchange Service (Deutscher Akademischer Austauschdienst DAAD) project number 57446513. This project received funding from the European Research Council (ERC) under the European Union's Horizon 2020 research and innovation programme (Grant agreement No. 816006). BER and DH thank the German Research Foundation (Deutsche Forschungsgemeinschaft, DFG) for funding through the Centre for Excellence *liv*MatS Exec 2193/1 – 390951807 and the Baden-Württemberg Stiftung gGmbH (BiofMo-2, 3D Mosaic).

References

1 J. Chapman and F. Regan, *Adv. Eng. Mater.*, 2012, **14**, B175–B184.
2 S. Farhadi, M. Farzaneh and S. A. Kulinich, *Appl. Surf. Sci.*, 2011, **257**, 6264–6269.
3 X. Zhao, L. Li, B. Li, J. Zhang and A. Wang, *J. Mater. Chem. A*, 2014, **2**, 18281–18287.
4 E. C. Cho, C. W. Chang-Jian, H. C. Chen, K. S. Chuang, J. H. Zheng, Y. S. Hsiao, K. C. Lee and J. H. Huang, *Chem. Eng. J.*, 2017, **314**, 347–357.
5 A. Marmur, *Langmuir*, 2004, **20**, 3517–3519.
6 X. D. Zhao, G. Q. Xu and X. Y. Liu, in *Bioinspiration: From Nano to Micro Scales*, ed. X. Y. Liu, Springer, New York, NY, 2012, pp. 331–378.
7 W. Barthlott, T. Schimmel, S. Wiersch, K. Koch, M. Brede, M. Barczewski, S. Walheim, A. Weis, A. Kaltenmaier, A. Leder and H. F. Bohn, *Adv. Mater.*, 2010, **22**, 2325–2328.
8 J. Busch, W. Barthlott, M. Brede, W. Terlau and M. Mail, *Philos. Trans. R. Soc., A*, 2019, **377**, 20180263.
9 M. N. Kavalenka, F. Vüllers, S. Lischker, C. Zeiger, A. Hopf, M. Röhrig, B. E. Rapp, M. Worgull and H. Hölscher, *ACS Appl. Mater. Interfaces*, 2015, **7**, 10651–10655.
10 Y. Wang, Y. Shi, L. Pan, M. Yang, L. Peng, S. Zong, Y. Shi and G. Yu, *Nano Lett.*, 2014, **14**, 4803–4809.
11 A. Pozzato, S. D. Zilio, G. Fois, D. Vendramin, G. Mistura, M. Belotti, Y. Chen and M. Natali, *Microelectron. Eng.*, 2006, **83**, 884–888.
12 S. Martin and B. Bhushan, *J. Colloid Interface Sci.*, 2017, **488**, 118–126.
13 L. Feng, Z. Zhang, Z. Mai, Y. Ma, B. Liu, L. Jiang and D. Zhu, *Angew. Chem., Int. Ed.*, 2004, **43**, 2012–2014.
14 C. R. Crick, J. A. Gibbins and I. P. Parkin, *J. Mater. Chem. A*, 2013, **1**, 5943–5948.
15 C.-T. Hsieh, W.-Y. Chen and F.-L. Wu, *Carbon*, 2008, **46**, 1218–1224.
16 N. J. Shirtcliffe, G. McHale, M. I. Newton and C. C. Perry, *Langmuir*, 2003, **19**, 5626–5631.
17 H. Liu, L. Feng, J. Zhai, L. Jiang and D. Zhu, *Langmuir*, 2004, **20**, 5659–5661.
18 D. Helmer, N. Keller, F. Kotz, F. Stolz, C. Greiner, T. M. Nargang, K. Sachsenheimer and B. E. Rapp, *Sci. Rep.*, 2017, **7**, 1–6.
19 J. T. Han, Y. Zheng, J. H. Cho, X. Xu and K. Cho, *J. Phys. Chem. B*, 2005, **109**, 20773–20778.
20 A. Priola, R. Bongiovanni, G. Malucelli, A. Pollicino, C. Tonelli and G. Simeone, *Macromol. Chem. Phys.*, 1997, **198**, 1893–1907.
21 H. Teng, *Appl. Sci.*, 2012, **2**, 496–512.
22 P. Fabbri and M. Messori, in *Modification of Polymer Properties*, ed. C. F. Jasso-Gastinel and J. M. Kenny, William Andrew Publishing, 2017, pp. 109–130.
23 X. Mu, T. Bertron, C. Dunn, H. Qiao, J. Wu, Z. Zhao, C. Saldana and H. J. Qi, *Mater. Horiz.*, 2017, **4**, 442–449.
24 R. K. Kankala, X.-M. Xu, C.-G. Liu, A.-Z. Chen and S.-B. Wang, *Polymers*, 2018, **10**, 807.
25 L. Alison, S. Menasce, F. Bouville, E. Tervoort, I. Mattich, A. Ofner and A. R. Studart, *Sci. Rep.*, 2019, **9**, 409.
26 T. F. Pereira, M. F. Oliveira, I. A. Maia, J. V. L. Silva, M. F. Costa and R. M. S. M. Thiré, *Macromol. Symp.*, 2012, **319**, 64–73.

27 L. Alison, S. Menasce, F. Bouville, E. Tervoort, I. Mattich, A. Ofner and A. R. Studart, *Sci. Rep.*, 2019, **9**, 409.
28 X. Mu, T. Bertron, C. Dunn, H. Qiao, J. Wu, Z. Zhao, C. Saldana and H. J. Qi, *Mater. Horiz.*, 2017, **4**, 442–449.
29 R. Karyappa, A. Ohno and M. Hashimoto, *Mater. Horiz.*, 2019, **6**, 1834–1844.
30 K.-M. Lee, H. Park, J. Kim and D.-M. Chun, *Appl. Surf. Sci.*, 2019, **467–468**, 979–991.
31 S. Yuan, D. Strobbe, X. Li, J.-P. Kruth, P. Van Puyvelde and B. Van der Bruggen, *Chem. Eng. J.*, 2020, **385**, 123816.
32 J. Lv, Z. Gong, Z. He, J. Yang, Y. Chen, C. Tang, Y. Liu, M. Fan and W.-M. Lau, *J. Mater. Chem. A*, 2017, **5**, 12435–12444.
33 S. Yuan, D. Strobbe, J.-P. Kruth, P. V. Puyvelde and B. V. der Bruggen, *J. Mater. Chem. A*, 2017, **5**, 25401–25409.
34 B. Kang, J. Hyeon and H. So, *Appl. Surf. Sci.*, 2020, **499**, 143733.
35 Z. Zhou, L. Liu and W. Yuan, *New J. Chem.*, 2019, **43**, 15823–15831.
36 H. Mao, J. Tang, J. Chen, J. Wan, K. Hou, Y. Peng, D. M. Halat, L. Xiao, R. Zhang, X. Lv, A. Yang, Y. Cui and J. A. Reimer, *Sci. Adv.*, 2020, **6**, eabb0694.
37 J. Nunes-Pereira, S. Ribeiro, C. Ribeiro, C. J. Gombek, F. M. Gama, A. C. Gomes, D. A. Patterson and S. Lanceros-Méndez, *Polym. Test.*, 2015, **44**, 234–241.
38 M. Lebourg, J. S. Antón and J. L. G. Ribelles, *Eur. Polym. J.*, 2008, **44**, 2207–2218.
39 R. H. Schmidt, K. Mosbach and K. Haupt, *Adv. Mater.*, 2004, **16**, 719–722.
40 S. Biria and I. D. Hosein, *ACS Appl. Mater. Interfaces*, 2018, **10**, 3094–3105.
41 F. Wang, P. Altschuh, L. Ratke, H. Zhang, M. Selzer and B. Nestler, *Adv. Mater.*, 2019, **31**, 1806733.
42 S. Kato and A. Sato, *J. Mater. Chem.*, 2012, **22**, 8613–8621.
43 F. Kotz, P. Risch, D. Helmer and B. E. Rapp, *Adv. Mater.*, 2019, **31**, 1805982.
44 D. G. Moore, L. Barbera, K. Masania and A. R. Studart, *Nat. Mater.*, 2020, **19**, 212–217.
45 B. Deore, K. L. Sampson, T. Lacelle, N. Kredentser, J. Lefebvre, L. S. Young, J. Hyland, R. E. Amaya, J. Tanha, P. R. L. Malenfant, H. W. de Haan and C. Paquet, *Nat. Commun.*, 2021, **12**, 55.
46 Z. Dong, H. Cui, H. Zhang, F. Wang, X. Zhan, F. Mayer, B. Nestler, M. Wegener and P. A. Levkin, *Nat. Commun.*, 2021, **12**, 247.
47 F. Mayoussi, E. H. Doeven, D. Helmer and B. E. Rapp, in *Microfluidics, BioMEMS, and Medical Microsystems XIX*, International Society for Optics and Photonics, 2021, vol. 11637, p. 116370E.

